

Intraoperative ultrasound for guidance and tissue shift correction in image-guided neurosurgery

Roch M. Comeau^{a)}

McConnell Brain Imaging Center, Montreal Neurological Institute and Department of Biomedical Engineering, McGill University, Montreal, Quebec H3A 2B4, Canada

Abbas F. Sadikot

Department of Neurology and Neurosurgery, Montreal Neurological Institute, McGill University, Montreal, Quebec H3A 2B4, Canada

Aaron Fenster

Imaging Research Labs, The John P. Robarts Research Laboratories, University of Western Ontario, London, Ontario N6A 5K8, Canada

Terry M. Peters

Imaging Research Labs, The John P. Robarts Research Laboratories, University of Western Ontario, London, Ontario N6A 5K8, Canada and McConnell Brain Imaging Center, Montreal Neurological Institute, McGill University, Montreal, Quebec H3A 2B4, Canada

(Received 9 September 1999; accepted for publication 11 January 2000)

We present a surgical guidance system that incorporates pre-operative image information (e.g., MRI) with intraoperative ultrasound (US) imaging to detect and correct for brain tissue deformation during image-guided neurosurgery (IGNS). Many interactive IGNS implementations employ pre-operative images as a guide to the surgeons throughout the procedure. However, when a craniotomy is involved, tissue movement during a procedure can be a significant source of error in these systems. By incorporating intraoperative US imaging, the target volume can be scanned at any time, and two-dimensional US images may be compared directly to the corresponding slice from the pre-operative image. Homologous points may be mapped from the intraoperative to the pre-operative image space with an accuracy of better than 2 mm, enabling the surgeon to use this information to assess the accuracy of the guidance system along with the progress of the procedure (e.g., extent of lesion removal) at any time during the operation. Anatomical features may be identified on both the pre-operative and intraoperative images and used to generate a deformation map, which can be used to warp the pre-operative image to match the intraoperative US image. System validation is achieved using a deformable multi-modality imaging phantom, and preliminary clinical results are presented. © 2000 American Association of Physicists in Medicine. [S0094-2405(00)01404-8]

Key words: image-guided surgery, ultrasound, tissue deformation, image warping, image registration, neurosurgery, intraoperative imaging

I. INTRODUCTION

A. Image-guided neurosurgery (IGNS)

Radiological images have been used as a guide in neurosurgery for decades. Soon after their introduction by Roentgen, surgeons took advantage of this new form of information to better plan and perform surgical procedures. In 1918, Aubrey Mussen¹ built a stereotactic frame designed for human use. However, it was not until 30 years later (after his death) that this device was re-discovered. Subsequently, Spiegel and Wycis in 1947 further developed this technique of stereotaxy, which involved the use of a three-dimensional Cartesian coordinate system for the human brain. These coordinates were defined with respect both to the brain and radiographic images that were acquired with a reference (or stereotactic) frame attached to the patient's head.

Although the stereotactic frame is still in use for many surgical procedures,^{2,3} particularly where high accuracy and precision is required in the localization of targets, other techniques have recently been developed to provide more flex-

ible and interactive means of relating structures within the brain to images obtained pre-operatively. This field has become known as interactive image guided neurosurgery (IGNS).⁴⁻¹¹ IGNS enables the surgeon to navigate within the patient's brain using pre-operative images as a guide, by using a handheld computer-tracked probe or other instruments during the procedure in the operating room (OR). Following a calibration procedure, three-dimensional position and orientation of such a probe may be relayed to a computer and displayed within the three-dimensional pre-operative image.

Many investigators have described IGNS systems that use pre-operative anatomical images, including magnetic resonance imaging (MRI), computed tomography (CT) and digital subtraction angiography (DSA), as a navigational guide.¹² In addition to anatomical information, others have described systems that incorporate functional information in the form of positron emission tomography (PET) and functional magnetic resonance imaging (fMRI) to improve the information content used for neuro-navigation.^{13,14}

All of these systems relate the real-world coordinates of the patient to those of the pre-operative images using a rigid body transformation. This transformation is calculated either by identifying implanted markers,^{15–18} or external features on both the patient and anatomical images and employing a least squares minimization procedure to determine the spatial transformation between the two sets of data. Alternatively, a similar result may be achieved by sampling a series of points on the skin surface with a probe or optical scanning system, and calculating the transform that best fits these points to a segmented representation of the skin derived from the images.¹⁹

B. Accuracy considerations in IGNS

There are several sources of error associated with IGNS systems, all of which lead to the position of the tracked probe being incorrectly reported in relation to the images being used for guidance. These errors can be linked to the failure of two basic assumptions:

- (1) that the equipment, registration and images are perfectly accurate, i.e., the pointer tracking device is free of positioning error, the registration between the patient and image spaces is error free, and that the images are free from spatial distortion; and,
- (2) that the equipment and volume of interest form a completely rigid system, i.e., the structures of interest within the brain remain in the same position with respect to the external fiducial points used for patient-image registration and the tracking device throughout the procedure.

Commercially available tracking devices can provide position and orientation information with sub-millimeter accuracy. Simple point matching, where homologous point-pairs are identified manually in the images and on the patient, followed by a least-squares distance minimization technique, can yield patient-image coordinate mapping with accuracy on the order of 2–3 mm.²⁰ MRI (the most common image modality used in IGNS) image distortion is highly dependent on acquisition parameters and is the subject of investigation in our laboratory.²¹ Geometric distortion can be in the order of 2–5 mm if no precautions are taken to avoid it.^{22–24}

During a neurosurgical procedure, the patient's head is generally rigidly fixed to the operating table using a clamp that immobilizes the skull using compression pins. Either the tracker itself, or a tracked reference object, is attached directly to the head fixation device forming a rigid system consisting of the patient's skull, the fixation device and the tracker. During open craniotomies, the release of intracranial pressure, the effect of gravity and drugs, and the resection of tissue, cause the brain to distort with respect to the skull, and more importantly, the external registration points. IGNS systems based on pre-operative information cannot account for this movement which is often in the order of 15 mm, and can exceed 25 mm.^{25,26}

C. Intraoperative mapping of brain movement

In order to measure the extent of brain shift, a means of acquiring anatomical images of the brain after it has shifted is required. This problem may be approached in two ways: The shape of the exposed brain can be tracked by sampling its surface with a physical pointer or by using a range sensor, or alternatively, by acquiring tomographic information using an intraoperative imaging device, either MRI or ultrasound (US).

1. Cortical surface movement measurement

One of the first indications of brain shift is the visible movement of the cortical surface after performing a craniotomy. The most obvious way to quantify such tissue movement is by measuring the position of the cortical surface, and comparing this to the surface derived from the pre-operative data. The simplest approach is to use the IGNS probe to obtain discrete samples of the surface, and to map these to homologous points on the pre-operative data.²⁵ Other investigators have approached this task by using the focal point of a tracked operating microscope as a virtual probe tip.²⁶

In addition to sampling discrete points on the cortical surface, another surface based approach is to obtain cortical surface range images, either using stereo image pairs, or a range sensor. Such a device, whose position is known in the tracker frame of reference, can be used to obtain profiles of the cortical surface. These profiles, combined with a finite element model approach can be employed to estimate the movement of structures below the surface itself.²⁷

2. Tomographic measurement: Intraoperative MRI

Although intraoperative MRI can provide excellent images of the brain's anatomical structures^{28–30} and is being used to study brain deformation,³¹ it has its limitations. First, a dedicated intraoperative MRI system requires a substantial investment for the scanner itself as well as equipping the operating room with MR-compatible instruments. In addition, the physical layout of many interventional MRI systems compromises the surgeon's access to the operating field.

3. Tomographic measurement: Intraoperative ultrasound

Intraoperative US provides images that have little distortion, does not require a dedicated machine, and costs less than 10% of a typical MRI system. US systems are portable, enabling them to be shared, have few special logistical requirements and are compatible with existing OR equipment. US has a long established track record for intraoperative use in neurosurgery.^{32–40} Intraoperative US can be used to acquire images of the anatomy (B-mode) and of the vasculature (Color Doppler and Power Doppler) at any time during the operation. This information, if correlated to the pre-operative data, can be used directly to measure and correct for brain shift.

D. Ultrasound in surgical guidance

In order to use intraoperative US to study brain deformation that occurs during surgery, the images must be acquired so as to allow the mapping of the pixels in the intraoperative US images to homologous locations in the pre-operative images. This requires that a means of determining the position and orientation of the US image with respect to the pre-operative image be established. In 1994, Trobaugh *et al.* introduced the concept of correlating intraoperative US with pre-operative CT or MRI, by monitoring the position and orientation of the US transducer with a tracking device.^{41,42} Since then, others have developed techniques to either compare 2D ultrasound images to other modalities,^{43–45} or to accumulate a series of ultrasound images to create volumetric data sets.^{46–49}

Each of these techniques requires that the coordinate transformation from the US image space to the pre-operative image space be established. This is accomplished using a 3D tracking device or articulated arm attached to a stereotactic frame. The relationship between the US image and the tracker/stereotactic coordinate space is determined *a priori* by performing a calibration procedure. Generally, this process requires that the operator obtain US images of a special imaging phantom, containing one or more targets at known locations in space. These targets typically consist of small, suspended beads or wire crosses. An assumption is made that the operator can position the transducer in such a way that the target is in the center of the US image slice. Prager *et al.* introduced a novel calibration phantom and technique to obtain this calibration automatically.⁵⁰ In addition, various techniques for acquiring and displaying 3D (volumetric) ultrasound data have recently been described in the literature, and many of these have direct relevance to the acquisition of intraoperative US images.^{51,52}

E. Our approach

Our goal is to provide the surgeon with the ability to compare both the pre- and intraoperative information in real-time during a neurosurgical procedure. To achieve this we have combined qualitative and quantitative approaches to this problem. We provide tools to enable the surgeon to qualitatively assess the presence of intraoperative brain shift, quantitatively measure this shift, and then use the information to deform or “warp” the pre-operative images, effectively realigning them to the US image.

The first step toward achieving any of the above goals is to determine the position and orientation of an ultrasound image in the coordinate space defined by the pre-operative image.

In the following discussion, we refer to various “spaces” as illustrated by Fig. 1. Each defines a Cartesian coordinate system attached to a system component, i.e., the tracked probe, the probe holder, the patient, or the patient’s images. These coordinate systems may be related to each other using 4×4 transformation matrices. These can either be rigid body transformations, including rotation and translation, or affine

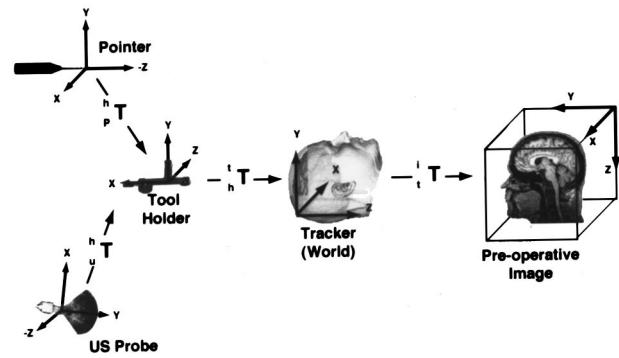


FIG. 1. Illustration of the coordinate systems and transformations relating them to each other.

transformations which are rigid body with the addition of scaling.

Referring to Fig. 1, and assuming that the brain and skull form a rigid body, any point p_i in pre-operative image space can be represented as a point p_u in intraoperative US image space with the relation:

$$p_i = p_u \cdot {}^hT \cdot {}^tT \cdot {}^iT,$$

where hT is the affine transformation from US image to tool holder space, tT is the rigid body transformation from tool holder to the tracker origin, and iT is the affine transformation from tracker to pre-operative patient image space. tT is obtained from the tracking device, iT is derived using one of the patient-image registration procedures described earlier, and hT is calculated via the calibration procedure described below.

II. MATERIALS AND METHODS

A. Calibration procedure

The components of the matrix (hT) describing the transformation from ultrasound image to tool holder space is determined using a calibration phantom which allows us to calculate the position of fiducial markers with respect to the phantom frame of reference (p_p). The phantom itself has holes milled into it at known locations, so that the location of the phantom in tracker space (tT) can be determined by identifying these points using a pointer attached to the tracker. If the ultrasound transducer is attached to the tracker during acquisition, then tT (and thus hT) is known for each acquired image. With this information, the location of fiducial markers of any image can be expressed in a common probe-holder space by:

$$p_h = p_p \cdot {}^tT \cdot {}^hT.$$

Thus we have the relation:

$$p_u \cdot {}^hT = p_h.$$

With p_h and p_u , hT can be determined using a least squares fitting technique.⁵³ This procedure allows for multiple im-

ages of the phantom, and thus many fiducial points to be accumulated and used in the calculation of h_uT .

B. Ultrasound phantoms

Two phantoms were used to first calibrate and later validate our US based IGNS system. The calibration phantom is required to determine the transformation between the ultrasound image and the tracking device attached to the ultrasound transducer (h_uT). The second phantom was employed to simulate brain deformation, and thus allow us to test the system's ability to detect and correct for this deformation.

1. Phantom material poly (vinyl alcohol) cryogel (PVA-C)

For the work described here, we required a phantom that would be robust and stable over time, simulate the imaging characteristics of brain tissue with US, MRI and CT, and to exhibit mechanical characteristics that are close to that of the human brain.

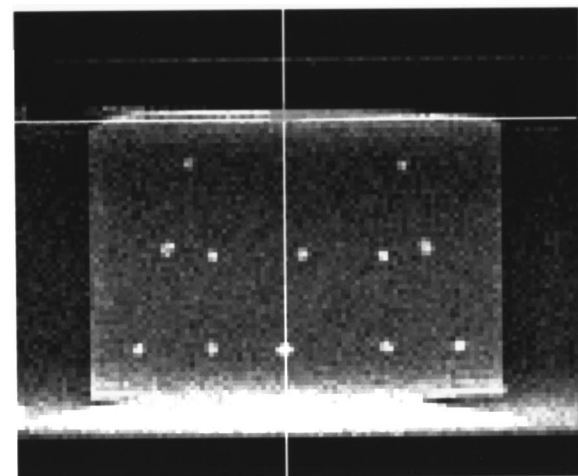
PVA-C⁵⁴ provides these qualities. This material is first prepared as a viscous fluid, which is then poured into a mold, and subjected to repeated freeze/thaw cycles. The mechanical properties of the PVA-C (along with the T1 and T2 MRI characteristics) may be controlled by varying the PVA-C/water concentration on the original mixture, as well as by changing the number of freeze–thaw cycles to which the mixture is subsequently exposed. Provided the material is stored in a humid environment, it appears to be stable over time (at least 3 years, in our experience).

2. Calibration phantom

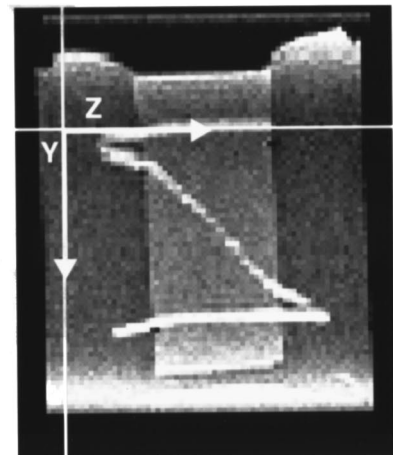
Our present calibration phantom is an improvement on previous work.⁵⁵ Its design follows that of a stereotactic frame, in that it defines a coordinate space, and contains fiducial markers that allow the locations of tomographic images to be determined within this space. It is constructed of PVA-C and contains 4 Z-bar fiducial markers (Fig. 2). The intersection of the three segments of the Z-bar with the image plane appear as three dots on the image. The principle of similar triangles along with the known location of the Z-bar in the phantom's coordinate space is used to calculate the location of the center marker within the phantom. Using the four Z-bars, four sets of homologous points in both the phantom and the image coordinate space are obtained. This fiducial marker configuration permits the position of the center of the US slice to be determined, and is thus relatively immune to variations in slice thickness.

3. Deformation phantom

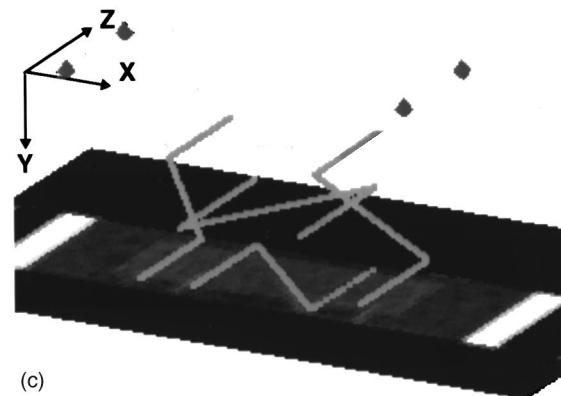
This phantom was constructed to allow us to image simulated tissue components with both MRI and US, under both standard and deformed conditions. The phantom consists of a PVA-C disk [Fig. 3(a)], a supporting collar, and a water bath container [Fig. 3(b)]. The disk was constructed by creating two hemisphere molds which have ridged outer edges to simulate cortical surfaces, as well as fluid compartments to simulate blood vessels and ventricles. These molds were



(a)



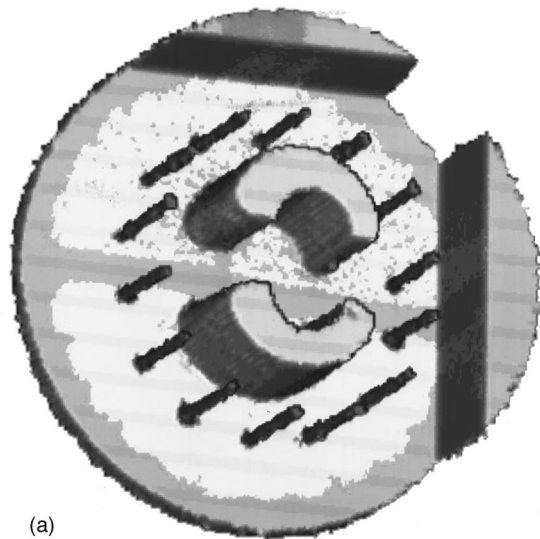
(b)



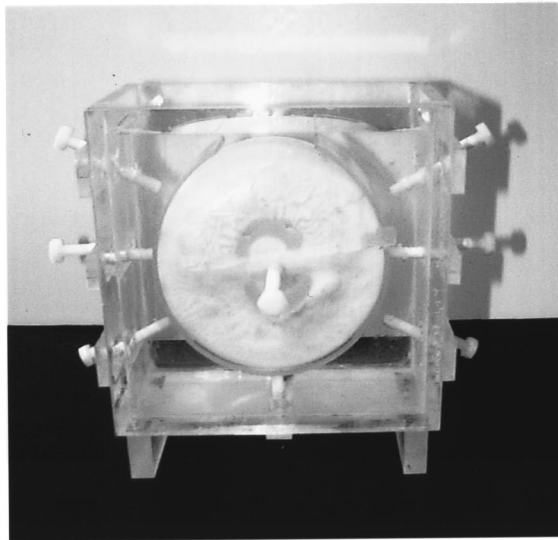
(c)

Fig. 2. Images of the “stereotactic” calibration phantom. (a) Coronal MPR displaying a cross sectional view of the Z-markers. (b) Oblique MPR view of an MRI of the phantom displaying one of the Z-bar markers. (c) 3D surface rendering of the Z-bars within the phantom (gray bars) and the locations of the holes milled into the phantom box (gray dots).

filled with PVA-C (10% PVA/vol) and subjected to a single freeze/thaw cycle. These hemispheres were removed from the mold and placed symmetrically in a larger cylindrical mold. The gaps between the hemispheres and the cylinder



(a)



(b)

FIG. 3. (a) 3D reconstruction of the PVA disk, demonstrating the simulated cortical surfaces, blood vessels and ventricles. (b) PVA disk and support collar immersed in the water bath container. The support screws protruding into the container support the collar and allow for deformation of the phantom by altering their tension.

wall were filled with additional PVA (15%/vol) and subjected to another freeze/thaw cycle. The contrast generated by both the differences in PVA-C concentration and the number of freeze/thaw cycles between the various components within the phantom provided MRI contrast of the simulated cortical surface and a “mid-line” between the “hemispheres.” These edges and fluid compartments were visualized in both MRI and US. The disk is partially surrounded by a Plexiglas collar for support while allowing a window for ultrasound imaging. The disk and collar are immersed in a 5% glycerin bath for both MRI and US imaging. The phantom can be deformed in a controlled manner by adjusting any of the seven screws which protrude into the container to support the collar and the phantom.

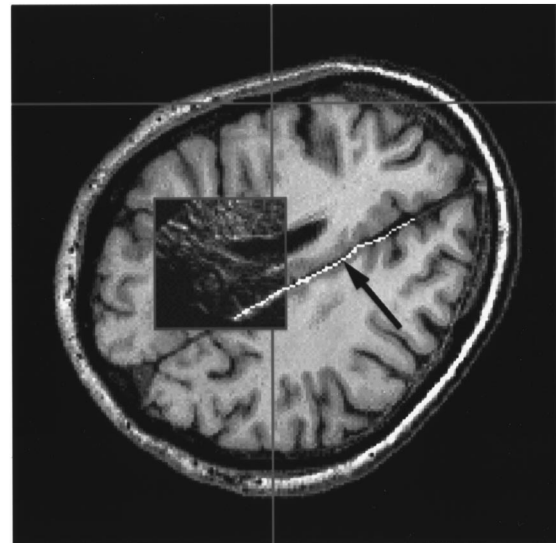


FIG. 4. Oblique MR image demonstrating qualitative visualization tools to assess brain shift: Co-planar intraoperative US image overlaid within an interactive region of interest (ROI box). Mid-line (falx) delineated by drawing a smooth cubic-spline curve (arrow) on MRI and displayed on both the MRI and on the homologous US image (shown within the ROI). The curve can also be displayed on the US image itself (not shown).

C. System description

Our navigation system consists of an ATL Ultramark 9 ultrasound system with a P7-4 multi-frequency probe (Advanced Technologies Laboratories Inc., Bothwell, WA). The probe is attached to a six degree of freedom tracking device, either a Surgicom articulated arm (FARO Technologies, Lake Mary, FL), or a Polaris freehand optical tracking system (Northern Digital, Waterloo, ON). Both systems monitor the position and orientation of a probe holder, to which tools are attached (e.g., pointer, transducer). The NTSC video output of the US system is connected to a frame grabber on a Macintosh G3 workstation (Apple Computer, Cupertino, CA). During image acquisition, the workstation obtains the position and orientation of the probe holder from the tracker via the serial port. Our IGNS software allows us to register the pre-operative data to the patient for general image guidance. Using the US calibration information, we can also display the live ultrasound data and the corresponding plane of pre-operative data simultaneously.

1. Qualitative display tools

The most basic data that can be provided to the surgeons is qualitative information that allows them to compare the pre- and intraoperative images. We provide both a region of interest (ROI) overlay tool, and a manual feature extraction tool to permit the comparison of co-planar views of the live US and pre-operative data.

The ROI tool allows the user to define a rectangular region that can overlay the US image on the MRI and vice versa (Fig. 4). This ROI can be moved over the image interactively with the computer mouse to obtain a qualitative appreciation of the differences of the two images.

The feature extraction tool allows the user either to drop individual markers or to draw spline-based curves on one of the co-planar images, and to display them on the homologous image (Fig. 4). This permits the delineation of point structures (e.g., blood vessels crossing the image plane) or boundaries (e.g., ventricles) from one image, and their locations to be visualized in the other image. These manually delineated structures can be stored and used to quantify and correct the deformation as described below.

2. Deformation quantification/correction tools

After visualizing any deformation, the next step is to quantify its extent and correct for it. We have incorporated tools that allow the surgeon to measure distances between homologous points in the pre- and intraoperative space, and use the feature extraction tool to delineate and compare homologous curves. Finally, these homologous points and curves can be used to determine a series of deformation vectors that can be propagated over a 2D grid to approximate the deformation over the entire image. This vector grid can be applied to the pre-operative data to deform it to better reflect the intraoperative geometry.

D. Operating room procedure

During surgery, the patient- and image-spaces are related by the rigid body transformation obtained by identification of homologous points, followed by application of the least-squares minimization technique discussed earlier. The selected features usually include the bridge of the nose, inner and outer canthi of the eyes, and the tragus of the ear. Visual verification is performed by placing the pointer on the skin surface at several points around the head, and observing the image location on the screen. If the location on the screen is off the skin by more than 2–3 mm the registration is repeated.

The US image acquisition configuration depends on the tracking system used. When employing the Faro arm, the ultrasound transducer is first placed in a sterile plastic bag and attached to a sterilized adapter, which in turn is attached to the tracking device (also in a sterile bag). When using the Polaris optical tracker, the transducer is attached to the optical emitters, and both are placed in a clear sterile bag. When images are acquired, the transducer is placed lightly on either the cortical surface or the dura (Fig. 5), with frequent irrigation with saline, or directly into the saline-filled surgical cavity after the initial resection. We point out that both the Faro and Polaris trackers have similar accuracy characteristics and perform the same tracking task. The advantage of the Faro arm is that it is mechanical and the probe is tracked under all circumstances. Its bulk nevertheless makes it somewhat intrusive in the operating room. The optical Polaris tracker is light and much less intrusive, but its major disadvantage is that it must always maintain sight-lines with the tracking cameras. The optically based tracker offers more maneuvering flexibility than mechanical arms, and better accuracy and reliability than magnetic position sensors⁵⁶ (another common tracking approach), particularly in the metallic environment of the operating room. The tracking system allows a tracked



Fig. 5. Ultrasound probe assembly during image acquisition on the cortex. The probe and Polaris tracker are in a transparent sterile bag. Ultrasound jelly is placed on the transducer head before insertion into the bag. The bag/cortex interface is kept irrigated with saline solution for acoustic coupling.

reference frame object to be attached to the skull clamp, permitting camera movement during the procedure without loss of registration.

After registration and skin incision, a series of points ($n \sim 25$) is sampled with the pointer on the skull surface. The skull points can be used to further evaluate the registration quality, although no correction is possible at this point. Following the craniotomy and after the dura has been opened, an additional point set is acquired over the surface of the cortex. Ultrasound images are also acquired by lightly placing the transducer on the cortical surface and applying irrigation for acoustic coupling.

III. RESULTS

A. System characterization—validation

1. Ultrasound calibration reproducibility

Ultrasound calibration results using the original calibration phantom for the Faro arm have been previously reported.⁵⁵ In order to verify that the US calibration transformation (${}^u_h T$) is reproducible for the optical tracker, four sets of calibration images (four images per set) were obtained at maximum imaging depth (MID) settings of 7 and 9 cm. The maximum imaging depth represents the distance from the transducer face to the most distal tissue displayed at the bottom of the screen. The phantom was localized in tracker

TABLE I. Results of the reproducibility study for the US image to tracker offset (the distance from the tracker origin to the US image origin in the tracker frame of reference) for two common US maximum imaging depth (MID) settings. Mean represents the average value for four calibration trials in the X, Y, and Z directions.

	Tracker to US image offset (mm)					
	7-cm MID			9-cm MID		
	X(mm)	Y(mm)	Z(mm)	X(mm)	Y(mm)	Z(mm)
Mean	-175.8	-35.7	-0.1	-175.6	-36.8	0.6
Maximum deviation	0.3	1.0	0.4	0.6	0.5	0.1

space, using a pointer attached to the tracker to identify holes milled into the support plates. With these, four probe calibrations were obtained for the two depths and compared.

Table I summarizes the reproducibility results. From these, it can be seen that the actual offset for either depth remains relatively unchanged, meaning that the origin of the US image is independent of the MID setting, and that any differences in the images are only the result of changes in pixel scaling.

2. Overall system accuracy target localization error (TLE)

In order to verify the overall system accuracy, a CT scan of the calibration phantom was obtained (pixel size=0.5 mm, slice thickness=1.5 mm, slice gap=1.5 mm) and used as a simulated pre-operative data set. The data were accurately registered to the phantom using the pointer to identify holes (filled with contrast agent during imaging) milled into the phantom, and a mouse to select their representations in the images. Once a satisfactory registration was obtained, the tracked US transducer was used to image the phantom. Five image pairs of both the US and the co-planar CT data were acquired for each imaging depth. The fiducial markers were identified on both the US and CT images, yielding 20 pairs of fiducial marker coordinates (per depth run) which were compared.

Table II summarizes the results from the determination of TLE. These demonstrate that with accurate fiducial marker registration, one can map an US image pixel to its homologous MRI pixel with an accuracy of ≤ 1.3 mm.

B. Deformation visualization/correction

1. Deformation visualization

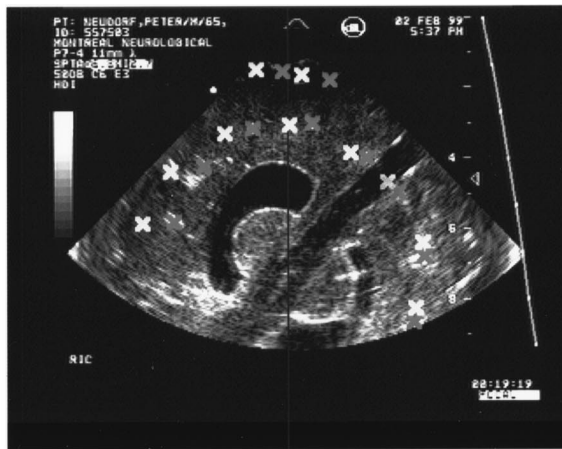
The PVA-C phantom was assembled and the screws initially set such that there was no deformation. MR images were obtained (T1-weighted gradient echo sequence, TR=14 ms, TE=6 ms, Flip angle=23 degrees, Averages=5) and transferred to the IGNS system. The phantom was then fixed on a table, and registered with the MRI data using the IGNS probe. Once an acceptable registration was obtained, US images were acquired and visualized with the IGNS software.

Without moving the phantom holder, the PVA-C disk was deformed by tightening the retaining screws in a diagonal fashion, creating a deformation of the ventricles and movement of the simulated cortical surface and blood vessels. The phantom was imaged again with the US system. The US and co-planar MR images were qualitatively compared using the interactive ROI tool to visualize the US superimposed on the MR images, and by delineating and visualizing the ventricles and blood vessels with the drawing tools. The deformation was assessed by measuring the distance between the homologous vessel points as represented on the MR and US images. The movements of the simulated blood vessels (within the US field of view) ranged from 3.7 to 9.4 mm. Images of both the nondeformed MRI and the US images of the deformed phantom were stored for later correction.

The phantom was imaged in the deformed state with the MRI using the previous parameters. An oblique image that was co-planar with the stored US/MRI image pair was obtained and stored so that MRI/US and MRI/MRI deformation detection could be compared. As before, structures were delineated in the deformed MRI image for examination.

TABLE II. Average differences (target registration error) in the x, y, z directions (phantom reference frame) and distance magnitude between the ultrasound and co-planar CT-derived fiducial marker coordinates ($n=20$), for US MID's of 7 and 9 cm.

	Target registration error							
	7-cm MID				9-cm MID			
	ΔX (mm)	ΔY (mm)	ΔZ (mm)	r (mm)	ΔX (mm)	ΔY (mm)	ΔZ (mm)	r (mm)
Mean	0.64	0.45	0.89	1.30	0.51	0.45	0.77	1.13
Standard deviation	0.64	0.58	0.64	0.92	0.53	0.62	0.61	0.91
Maximum deviation	2.29	2.16	2.15	3.13	1.82	2.01	1.92	2.80



(a)



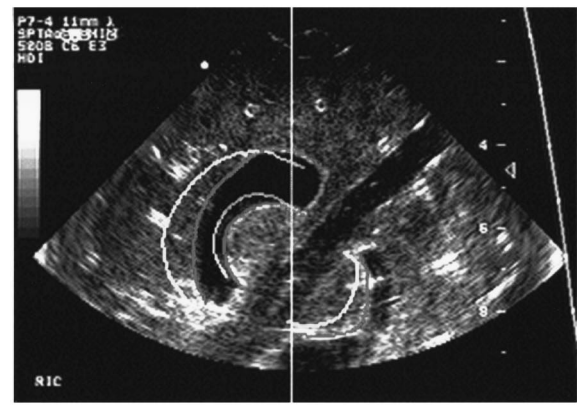
(b)

FIG. 6. US and co-planar MRI of deformable “brain” phantom before (MRI) and after (US) deformation. Dark markers indicate features identified on the US image, while light markers are homologous points identified on the MRI.

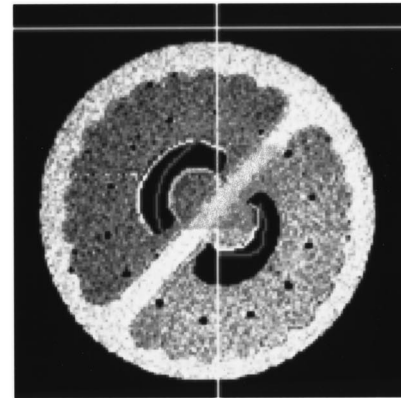
2. Deformation correction

One pair of images (one US and one coplanar MR image) was selected for deformation analysis. The phantom outline was obtained and the ventricles, simulated blood vessels and visible sulci were delineated as above on both images (Fig. 6 and Fig. 7). The phantom outline was employed to define the border of the deformation area. The ventricle outlines were then converted to a discrete set of deformation vectors by parametrically sampling the homologous spline curves to obtain a series of homologous point pairs, which were subsequently combined with some of the vessel point pairs to obtain a series of deformation vectors. Some vessel point pairs were deliberately left out of the calculations so that they could be used later to determine the TLE in the warped image. These vectors were then applied to a vector grid (64×64 nodes, of which only a subset is displayed in Fig. 8 for clarity) to obtain an initial deformation condition [Fig. 8(a)]. These initial deformations were linearly interpolated by propagating their values to their neighboring nodes using the following iterative technique.

Step 1: For each initial displacement vector, locate and ap-



(a)



(b)

FIG. 7. US and co-planar MRI of deformable “brain” phantom after deformation. Dark curves indicate ventricle boundaries identified from the US image while light curves are homologous curves derived from the MRI image.

ply the displacement to the nearest grid node.

Step 2: For each displaced node, notify neighboring nodes of the displacement.

Step 3: For each node notified of a neighbor’s movement, calculate a new displacement vector by taking the average displacement of all its neighbors, and flag itself as displaced.

Step 4: If either the maximum displacement is above the minimum stop threshold, or the iteration count is below a preset maximum, repeat from step 2, otherwise, stop.

A similar result would be expected using a thin plate spline algorithm.⁵⁷ Figure 8(b) shows the resulting deformation grid, which was applied to the original MR image yielding a piecewise linearly warped image (Fig. 9). The deformation for pixels between grid points was determined using linear interpolation. The visualization tools were then used to compare the US images with the warped MR image for discrepancies. Figure 9(a) shows the warped image with the ventricle curves derived from both the US image of the deformed phantom (dashed) and the nonwarped MRI (solid), and demonstrates good agreement between the US derived curves and the warped MRI. Figure 9(b) displays the warped, or realigned MRI with the US image shown within the ROI. The position of the simulated vessels seen in the upper quad-

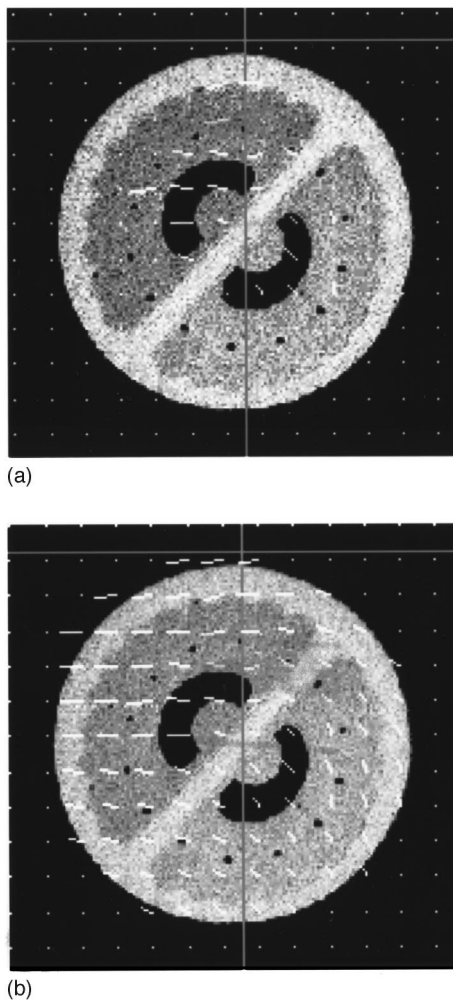


FIG. 8. Deformation grid superimposed on the nondeformed MRI (16×16 subset of 64×64 nodes displayed). (a) Grid with initial deformation vectors applied. (b) Deformation grid after propagation/relaxation of the initial deformation to the other nodes.

rant of the US ROI agree well with that of the homologous vessels in the warped MRI. The previously identified vessel point pairs that were not used to calculate the deformation grid were identified in the warped MR image, and comparison of their positions when seen in the ultrasound yielded discrepancies ranging from 0.7 to 2.0 mm, with an average of 1.3 mm.

The magnitude of the movement for each grid point was obtained and linearly interpolated to match its resolution to that of the MR image. Figure 10(a) shows the deformation magnitude superimposed as contours on the phantom structures for the MRI pre-deformation and US post-deformation derived grid.

The same procedure of delineating structures was performed in the post-deformation MR image, and deformation grids were obtained using the pre-deformed and post-deformed MR derived features. Figure 10(b) illustrates the resulting deformation magnitudes from one such calculation superimposed as contours on the nonwarped MRI. The deformation grid was then applied to the nondeformed MRI.

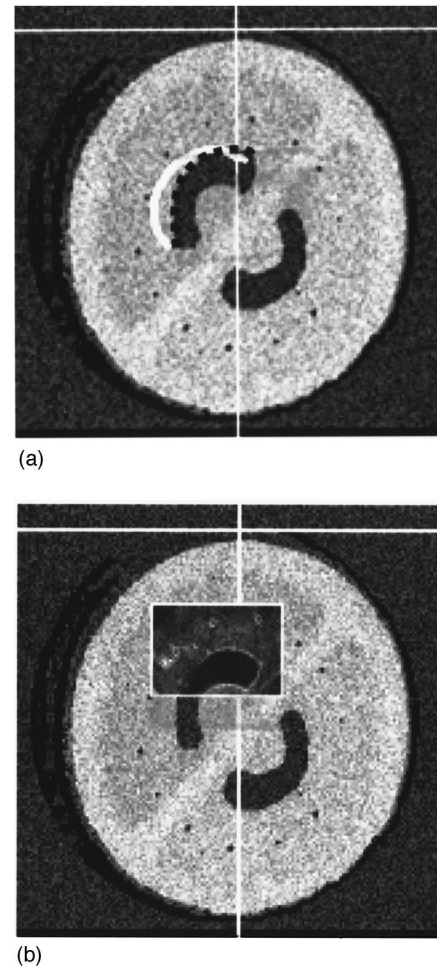


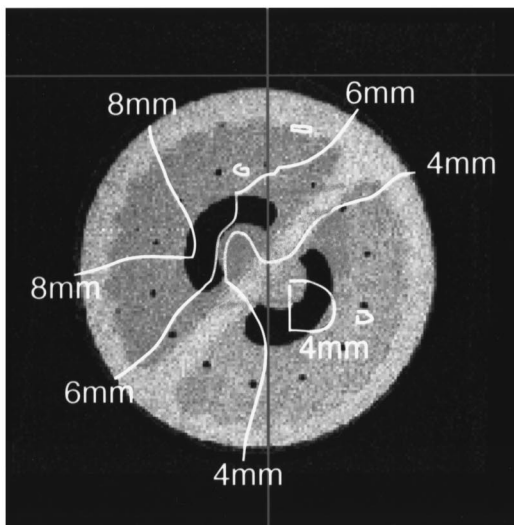
FIG. 9. (a) Deformed MRI image of phantom. The ventricular wall was manually delineated (solid curve) from the nondeformed MRI [Fig. 7(b)] to demonstrate the deformation (dashed line). (b) Deformed MRI image displayed with the US image within the ROI, showing good agreement of the simulated ventricular structures and the blood vessels. The outer wall of the ventricle in the deformed MRI conformed to the US ventricle wall to within 1.5 mm.

Visual comparison of the deformation magnitude contours from the US/MRI and MRI/MRI deformations show good agreement. The distances from the homologous simulated blood vessels in the deformed MRI and warped MRI were measured, and ranged from 0.5 to 1.9 mm, with an average value of 1.3 mm. Table III compares the average, maximum and minimum of the deformation magnitudes of all grid nodes, confirming agreement between the US/MRI and MRI/MRI derived values.

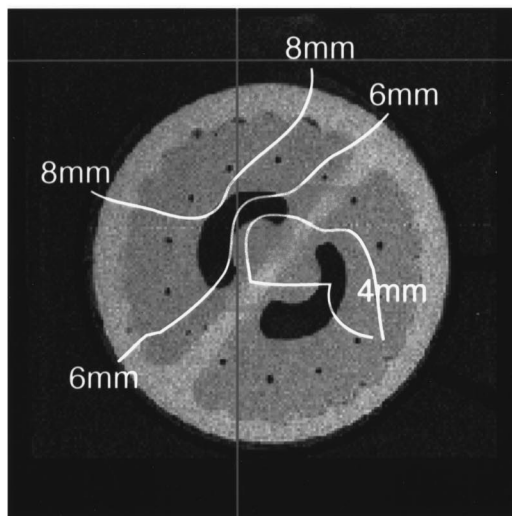
C. Intraoperative examples

1. Intraoperative case 1

The following example was a neurosurgical case involving the extension of a previous tumour resection. The MRI data set was registered to the patient, and surface points (skin, skull, dura and cortex) were acquired according to the protocol described above. The Polaris optical tracker was used to track both the pointer and the ultrasound transducer.



(a)



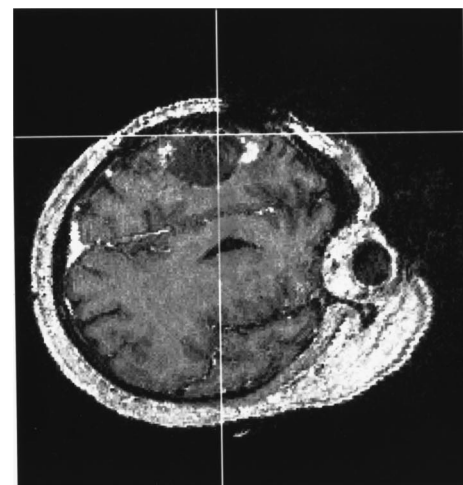
(b)

FIG. 10. Deformation distance (magnitudes) superimposed as contours on the nondeformed MRI of the deformation phantom. (a) Deformation obtained by comparing nondeformed MRI images to deformed US images. (b) Deformation obtained by comparing nondeformed and deformed MRI.

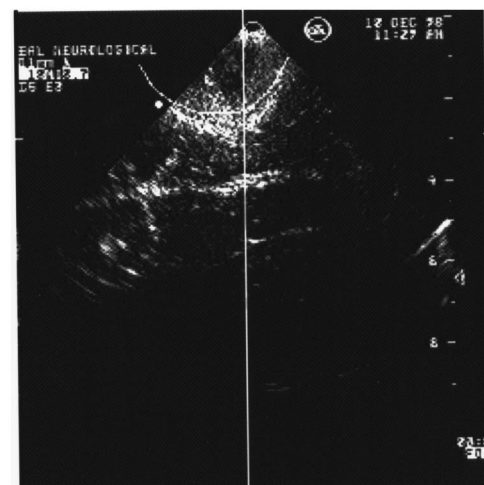
After image acquisition, the ROI tool was used to compare the US images to their co-planar MRI equivalents (Fig. 11). The surgeon was able to qualitatively assess the degree of brain shift by comparing the relative position of homologous structures, including the falx and the tumour boundary. The tumour boundary was manually delineated on the pre-

TABLE III. Grid node displacements obtained by comparing nondeformed MRI to the deformed US, and nondeformed MRI to the deformed MRI.

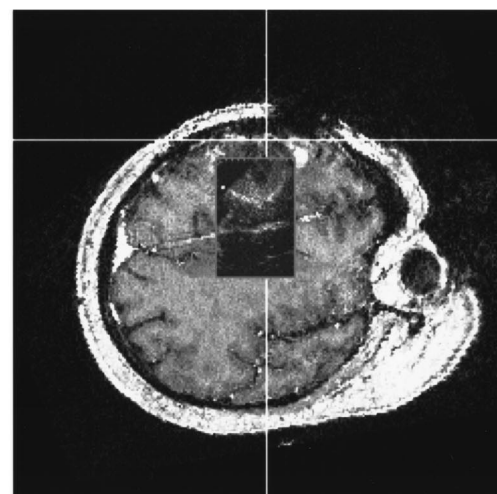
	Grid point displacements MRI-US (mm)	MRI-MRI (mm)
Average	5.45	5.88
Max	9.72	9.46
Min	2.71	2.25



(a)



(b)



(c)

FIG. 11. Comparison between pre-operative and intraoperative images during a tumour resection. (a) Gadolinium enhanced T1-weighted MRI reformatted to match the intraoperative US. (b) Intraoperative US image showing previous resection boundary and the mid-line (falx). Light curve (arrow) indicates resection boundary manually delineated from pre-operative MRI (a) (c) ROI tool display superimposing US onto co-planar MRI. Display shows good agreement in the mid-line structures while showing a suspected shift in the tumour boundaries.

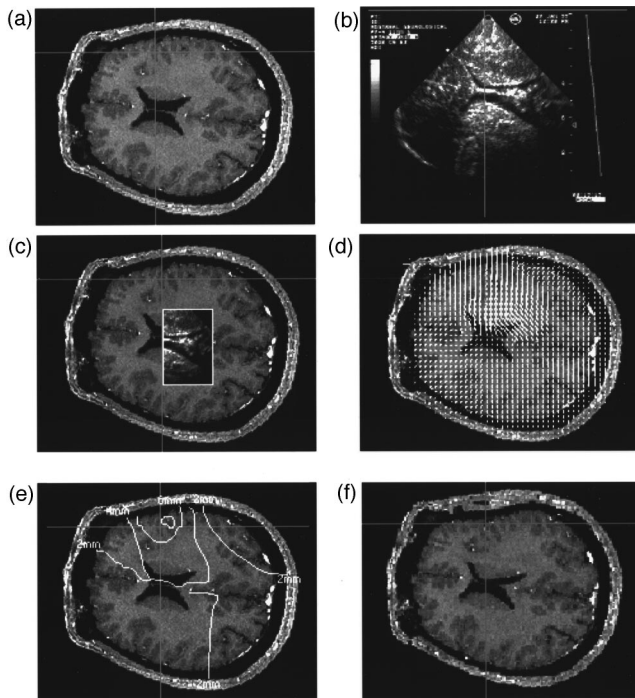


FIG. 12. (a) Oblique MRI image oriented to match intraoperative US image (b). The image clearly demonstrates the ventricles, mid-line (falx) and the cortical surface of the brain. (b) Intraoperative US image showing compressed ventricles, but relatively stable falx. (c) ROI tool superimposing intraoperative US on the pre-operative MRI demonstrating ventricular deformation. (d) Deformation grid ($n=64 \times 64$) obtained after delineation of the ventricles and the falx from the US image, and the cortical surface obtained from the point samples. (e) Deformation magnitude image obtained from the deformation grid. (f) Deformed MRI image after application of the deformation grid.

operative MR image using the feature extraction tool, and the resulting curve was overlaid on the US image to further assess the suspected tumour shift.

2. Intraoperative case 2

The second example is that of a neurosurgical procedure involving the partial resection of the hippocampus and the amygdala (selective amygdalo-hippocampotomy) for the treatment of intractable epilepsy. Patient registration and image acquisition were performed as described above, with the Polaris device again being used to track the pointer and ultrasound transducer.

Figure 12 shows relevant images from the case. It can be seen in A, B and C that while there has been contraction of the ventricles, the mid-line structures (falx) have remained relatively fixed. Figure 12(d) shows the displacement grid obtained by delineating the ventricles, falx and the skull from the pre-operative MRI and the intraoperative US, and the cortical surface delineated from the pre-operative MRI and the intraoperative sampled surface points. Thus, the US image is used to derive deformation information in depth while the discreet point samples are used to obtain deformation information of the brain surface. Figure 12(e) shows the deformation magnitude as interpreted from the US image

superimposed on the nondeformed MRI. It should be noted that the deformation information is only relevant within the field of view of the US transducer. Finally, Figure 12(f) shows the warped oblique MRI obtained by applying the deformation grid (d). The ventricular contraction as well as the “sinking” of the cortical surface is clearly demonstrated.

IV. DISCUSSION

A. Clinical usefulness

The primary goal of this project was to provide neurosurgeons with an IGNS system having practical tools to evaluate the extent of intraoperative brain shift and its effect on the accuracy of pre-operative images. The second goal was to apply quantitative methods to correct selected pre-operative images for the distortions.

To satisfy the first goal, real-time visualization tools were developed to allow the surgeon to acquire intraoperative US images, and to compare them to the pre-operative MR slices. The spatial tracking hardware was selected to provide good freedom of movement, and to minimize the intrusiveness of the tracking hardware on the operating environment.

The ROI tool provides a fast and intuitive method of comparing the pre- and intraoperative images. In addition to the qualitative ROI tool, the delineation tools (markers and manual spline curves) allow more detailed and quantitative analysis to be performed on the images.

While the initial number of cases where the system was used is limited, it is worth noting that almost no movement of the falx, with respect to cortical structures on the contralateral side was observed in many of these cases. This agrees with intraoperative MRI studies³¹ as well as personal observation of the surgical staff. This finding may suggest that a convenient boundary condition may be employed in the deformation process, restricting the calculations to the hemisphere affected by the surgery. If this proves to be consistent, it will have to be accounted for in current finite element model based approaches in characterizing the deformation.⁵⁸ The dynamics of tissue movement are less clear in procedures involving the falx itself.

B. System limitations

Although these tools have proven to be useful to the surgeons, there are limitations that require consideration. (1) Inaccuracies may be introduced by the use of exclusively 2D images for measuring brain shift. (2) The overall system accuracy limits the resolution of movement that can be observed. (3) The anatomic features used to assess shift may differ in appearance in the two imaging modalities. (4) The area where deformation correction is relevant is limited to the neighborhood of the homologous features identified.

1. Using 2D images to detect 3D shift

The use of two-dimensional images to study an inherently three-dimensional tissue shift requires that we assume the movement occurs in a principal direction, and that we can

orient the intraoperative US image in such a way that this principal direction lies within the plane of the image, capturing the shift.

Other investigators have published preliminary results of cortical surface brain shift measurements^{26,59} and have found that the direction of gravity and the direction of the normal to the cortex have a major influence in the direction of brain shift after craniotomy. This intuitive situation is supported by personal observation. The US imaging plane can easily be selected to capture this motion. Furthermore, because the system can display images in real time, many planes parallel to the direction of gravity and normal to the cortical surface may be readily acquired and examined.

2. Accuracy considerations

The phantom-based validation results show that when the registration error is minimized, landmarks can be mapped from pre-operative to intraoperative image space to within a few millimeters. Other investigators have reported that registration error, or more importantly, the TLE⁶⁰ is highly dependent on fiducial localization error (FLE) and can vary between 2 and 5 mm. We also would expect a similar accuracy limit in our ability to detect brain deformation using the ROI and manual feature extraction tool. Since we can already detect deformations on the order of 10–20 mm on the cortical surface, this already represents a significant improvement. If higher accuracy is required for this procedure, or for any pre-operative image based IGNS, a more accurate registration method must be employed. When required, implanted fiducial markers may be used to lower the FLE and thus the TLE.¹⁶ The accuracy required of the IGNS system for a particular procedure is ultimately decided by the surgeon, who chooses the trade-off between desired accuracy and the invasiveness of the registration procedure. It is impossible to decouple the linear registration error from the nonlinear deformation of the brain. Therefore, in the case of the pre-operative image restoration procedure, the component of the registration error that lies in the plane of the US image will be detected and corrected along with the nonlinear brain deformation.

The calibration employed to determine the transformation from the US image to the tool holder reference frame assumes that the speed of sound in the phantom and the target (brain) are identical. In reality, the speed of sound in the PVA-C used in the phantom is 1535 m/s, while the speed of sound in the brain is approximately 1510 m/s.⁶¹ Unless explicitly corrected for, this assumption leads to a localization error of 1.6%, or 1 mm at an imaging depth of 6 cm. In addition, the differences of the speed of sound in the different tissues within the brain may lead to inaccuracies, but to a lesser extent than that caused by the PVA-C/average brain difference.

3. Anatomic feature selection

The question of anatomic feature matching is complex. The feature that generates diagnostic contrast must be the same for the two modalities employed. Certain structures, including the ventricular wall, the falx, the vessels and cor-

tical folds when visible in US (i.e., tissue/CSF interfaces) may be easily and reliably matched between MR, CT and US. The validity of other features, for example the tumour border as seen in US and infused MRI, must be examined before they can be reliably used as features for movement detection and correction. This must be taken into account when assessing brain shift.

The accuracy of the estimation of the deformation depends on the density of homologous features. The actual feature density in the image will vary from case to case, and thus so will the accuracy. The phantom studies presented here show the potential of this technique, while the second intraoperative case shows a more typical example.

C. Future work

There are several avenues still to be explored, including how to use and improve existing tools to increase our understanding of brain shift during surgery, and how to correct for its effect.

The existing system is currently being used on a regular basis in the operating room, and data from its use are being accumulated and correlated to help increase our general understanding of the nature of tissue shift.

This system is being improved by examining other methods to estimate and characterize the deformation (e.g., thin plate splines). Methods of characterizing the confidence of the estimation of deformation throughout the image based on feature density are being examined. This will allow us to better evaluate where the deformation correction is relevant. The system is also being augmented to enable the accumulation of multiple US images into a volumetric data set. Finally, techniques for automatically extracting homologous features from images made with the two modalities are being explored. These facilities will help us move toward our ultimate goal of automatically warping the pre-operative MR images to match the intraoperative US data.

ACKNOWLEDGMENTS

We would like to thank our colleagues of the Neuroimaging Laboratory at the Montreal Neurological Institute (MNI) and the Imaging Research Labs of the John P. Robarts Research Institute (RRI) for their insightful discussion and technical support. In particular, we thank Kathleen Surry for help in the construction of the calibration phantom, and Dr. Kenneth Chu for supplying the PVA-C. We thank Dr. André Olivier of the Department of Neurosurgery at the MNI for access to the operating room; the department of Radiology at the MNI for access to the ultrasound machine; and ATL Inc. for supplying the ultrasound transducer. This work was supported in part by the National Science and Engineering Council of Canada (Grant No. CPG0164606) and the Medical Research Council of Canada (Grant No. MT11540).

^{a)}Electronic mail: roch@bic.mni.mcgill.ca

¹C. Picard, A. Olivier, and G. Bertrand, "The first human stereotaxic apparatus. The contribution of Aubrey Mussen to the field of stereotaxis," *J. Neurosurg.* **59**, 673–676 (1983).

- ²P. St-Jean, A. F. Sadikot, L. Collins, D. Clonda, R. Kasrai, A. C. Evans, and T. M. Peters, "Automated atlas integration and interactive three-dimensional visualization tools for planning and guidance in functional neurosurgery," *Med. Imaging* **17**, 672–680 (1998).
- ³R. L. Jensen, J. L. Stone, and R. Hayne, "Use of the Horsley–Clarke stereotactic frame in humans," *Stereotactic & Functional Neurosurgery* **65**, 194–197 (1995).
- ⁴R. L. Galloway, R. J. Maciunas, W. A. Bass, and D. Crouch, "Optical device for interactive, image-guided neurosurgery," *Proceedings of the Annual Conference on Engineering in Medicine and Biology* **15**, 954–955 (1993).
- ⁵B. L. Davey, R. M. Comeau, C. Gabe, A. Olivier, and T. M. Peters, "Interactive stereoscopic image-guided neurosurgery," *SPIE Image Display* **2164**, 167–176 (1994).
- ⁶R. Evans, "VISLAN computer-aided surgery," *IEEE Review* **41**, 51–54 (1995).
- ⁷R. Kikinis *et al.*, "Computer-assisted interactive three-dimensional planning for neurosurgical procedures," *Neurosurgery* **38**, 640–649, discussion 649–651 (1996).
- ⁸N. Kiya, C. Dureza, T. Fukushima, and J. C. Maroon, "Computer navigational microscope for minimally invasive neurosurgery," *Minim. Invasive Neurosurg.* **40**, 110–115 (1997).
- ⁹Y. Masutani, T. Dohi, F. Yamane, H. Iseki, and K. Takakura, "Interactive virtualized display system for intravascular neurosurgery," *CVRMed MRCAS '97. First Joint Conference, Computer Vision, Virtual Reality and Robotics in Medicine and Medical Robotics and Computer Assisted Surgery Proceedings*, Springer Verlag (1997).
- ¹⁰K. R. Smith, K. J. Frank, and R. D. Bucholz, "The NeuroStation—a highly accurate, minimally invasive solution to frameless stereotactic neurosurgery," *Comput Med Imaging Graph* **18**, 247–256 (1994).
- ¹¹L. J. Zamorano, L. Nolte, A. M. Kadi, and Z. Jiang, "Interactive intraoperative localization using an infrared-based system," *Neurol. Res.* **15**, 290–298 (1993).
- ¹²T. M. Peters, C. J. Henri, P. Munger, A. M. Takahaski, A. C. Evans, B. Davey, and A. Olivier, "Integration of stereoscopic DSA and 3D MRI for image-guided neurosurgery," *Computerized Medical Imaging & Graphics* **18**, 289–299 (1994).
- ¹³R. L. Galloway, Jr., W. A. Bass, H. Senel, and S. Schreiner, "Enhanced interactive surgical guidance using both pre-operative and intraoperative imaging," *SPIE Medical Imaging*, **1897**, 69–77 (1993).
- ¹⁴T. M. Peters, R. Comeau, P. Munger, B. L. K. Davey, L. Pisani, A. Sadikot, and A. Olivier, "Image-guided Neurosurgery at the Montreal Neurological Institute," *Proceedings of the Annual International Conference of the IEEE Engineering in Medicine and Biology* **2**, 635–636 (1996).
- ¹⁵J. T. Lewis and R. L. Galloway, "Three-dimensional localization of implanted fiducial markers for interactive, image-guided surgery," *Proceedings of the Annual Conference on Engineering in Medicine and Biology*, **15**, 952–953 (1993).
- ¹⁶C. R. Maurer, Jr., J. M. Fitzpatrick, M. Y. Wang, R. L. Galloway, Jr., R.-J. Maciunas, and G. S. Allen, "Registration of head volume images using implantable fiducial markers," *IEEE Trans. Med. Imaging* **16**, 447–462 (1997).
- ¹⁷S. Schreiner, J. T. Lewis, G. S. Allen, and R. L. Galloway, "Technique for the three dimensional localization of implanted fiducial markers," *SPIE Med. Imaging* **2431**, 148–161 (1995).
- ¹⁸F. C. Vinas, L. Zamorano, and R. Buciu, Q. H. Li, F. Shamsa, Z. Jiang, and F. G. Diaz, "Application accuracy study of a semipermanent fiducial system for frameless stereotaxis," *Computer Aided Surgery* **2**, 257–263 (1997).
- ¹⁹W. E. L. Grimson, T. Lozano-Perez, S. J. White, W. M. Wells III, R. Kikinis, and G. J. Ettinger, "Automated registration for visualization in surgery," *Image Understanding Workshop, Proceedings, Morgan Kaufmann Publishers, Part 2* (1994).
- ²⁰E. Cuchet, J. Knoploch, D. Dormont, and C. Marsault, "Registration in neurosurgery and neuroradiotherapy applications," *J. Image Guided Surgery* **1**, 198–207 (1995).
- ²¹P. Munger, "Accuracy Considerations in MR Image-guided Neurosurgery," M.Sc. thesis, McGill University, 1994.
- ²²E. Alexander III, H. M. Kooy, M. van Herk, M. Schwartz, P. D. Barnes, N. Tarbell, R. V. Mulkern, E. J. Holupka, and J. S. Loeffler, "Magnetic resonance image-directed stereotactic neurosurgery: Use of image fusion with computerized tomography to enhance spatial accuracy," *J. Neurosurg.* **83**, 271–276 (1995).
- ²³C. R. Maurer, Jr., G. B. Aboutanos, B. M. Dawant, S. Gadamsetty, R. A. Margolin, R. J. Maciunas, and J. M. Fitzpatrick, "Effect of geometrical distortion correction in MR on image registration accuracy," *J. Comp. Assisted Tomography* **20**, 666–679 (1996).
- ²⁴T. S. Sumanaweera, J. R. Adler, G. H. Glover, P. F. Hemler, P. A. van den Elsen, D. Martin, and S. Napel, "Method for correcting magnetic resonance image distortion for frame-based stereotactic surgery, with preliminary results," *J. Image Guided Surgery* **1**, 151–157 (1995).
- ²⁵D. L. G. Hill, C. R. Maurer, R. J. Maciunas, J. A. Barwise, J. M. Fitzpatrick, and M. Y. Wand, "Measurement of intraoperative brain surface deformation under a craniotomy," *Neurosurgery* **43**, 514–528 (1998).
- ²⁶D. W. Roberts, A. Hartov, F. E. Kennedy, M. I. Miga, and K. D. Paulsen, "Intraoperative brain shift and deformation: A quantitative analysis of cortical displacement in 28 cases," *Neurosurgery* **43**, 749–760 (1998).
- ²⁷M. Audette and T. M. Peters, "Level-set segmentation and registration for computing intrasurgical deformations," *SPIE Image Processing* **3661**, 110–121 (1999).
- ²⁸J. F. Schenck *et al.*, "Superconducting open-configuration MR imaging system for image-guided therapy," *Radiology* **195**, 805–814 (1995).
- ²⁹T. M. Moriarty, R. Kikinis, F. A. Jolesz, P. M. Black, and E. Alexander, 3rd, "Magnetic resonance imaging therapy. Intraoperative MR imaging," *Neurosurg. Clin. N. Am.* **7**, 323–331 (1996).
- ³⁰C. R. Wirtz, M. M. Bonsanto, M. Knauth, V. M. Fronnier, F. K. Albert, A. Staubert, and S. Kunze, "Intraoperative magnetic resonance imaging to update interactive navigation in neurosurgery: Method and preliminary experience," *Comput. Aided Surg.* **2**, 172–179 (1997).
- ³¹C. R. Maurer, Jr. *et al.*, "Investigation of intraoperative brain deformation using a 1.5T interventional MR system: Preliminary results," *IEEE Trans. Med. Imaging* **17**, 817–825 (1998).
- ³²G. J. Dohrmann and J. M. Rubin, "Dynamic intraoperative imaging and instrumentation of brain and spinal cord using ultrasound," *Neurol. Clin.* **3**, 425–437 (1985).
- ³³L. M. Auer and V. van Velthoven, "Intraoperative ultrasound (US) imaging. Comparison of pathomorphological findings in US and CT," *Acta Neurochir.* **104**, 84–95 (1990).
- ³⁴J. C. Sutcliffe, "The value of intraoperative ultrasound in neurosurgery," *Br. J. Neurosurg.* **5**, 169–178 (1991).
- ³⁵L. M. Auer, "Ultrasound stereotaxic endoscopy in neurosurgery," *Acta Neurochir. Suppl.* **54**, 34–41 (1992).
- ³⁶P. Kumar, R. Sukthakar, B. J. Damany, J. Mishra, and A. N. Jha, "Evaluation of intraoperative ultrasound in neurosurgery," *Ann. Acad. Med. Singapore* **22**, 422–427 (1993).
- ³⁷J. Godard, G. Jacquet, R. Steimle, and A. Czorny, "Peroperative echography in neurosurgery. Its value and applications 10 years later," *Neurochirurgie* **39**, 182–187 (1993).
- ³⁸A. Gronningsaeter, G. Unsgard, S. Ommedal, and B. A. Angelsen, "Ultrasound-guided neurosurgery: A feasibility study in the 3–30 MHz frequency range," *Br. J. Neurosurg.* **10**, 161–168 (1996).
- ³⁹V. van Velthoven and L. M. Auer, "Practical application of intraoperative ultrasound imaging," *Acta Neurochir.* **105**, 5–13 (1990).
- ⁴⁰K. Yamakawa, T. Kondo, M. Yoshioka, and K. Takakura, "Ultrasound guided endoscopic neurosurgery—new surgical instrument and technique," *Acta Neurochir. Suppl.* **61**, 46–48 (1994).
- ⁴¹J. W. Trobaugh, W. D. Richard, K. R. Smith, and R. D. Bucholz, "Frameless stereotactic ultrasonography: Method and applications," *Computerized Medical Imaging & Graphics* **18**, 235–246 (1994).
- ⁴²J. W. Trobaugh, P. Kessman, D. Dietz, and R. Bucholz, "Ultrasound in image fusion: A framework and applications," *Proceedings of the IEEE Ultrasonics Symposium* **2**, 1393–1396 (1997).
- ⁴³J. Koivukangas, Y. Louhisalmi, J. Alakuijala, and J. Oikarinen, "Ultrasound-controlled neuronavigator-guided brain surgery," *J. Neurosurg.* **79**, 36–42 (1993).
- ⁴⁴R. M. Comeau, A. Fenster, and T. M. Peters, "Intraoperative US in interactive image-guided neurosurgery," *Radiographics* **17**, 1019–1027 (1998).
- ⁴⁵C. Giorgi and D. S. Casolino, "Preliminary clinical experience with intraoperative stereotactic ultrasound imaging," *Stereotactic & Functional Neurosurgery* **68**, 54–58 (1997).
- ⁴⁶R. Rohling, A. Gee, and L. Berman, "Automatic registration of 3D ultrasound images," *Ultrasound Med. Biol.* **24**, 841–854 (1998).

- ⁴⁷L. H. Monsein, A. Y. Razumovsky, S. J. Ackerman, H. J. Nauta, and D. F. Hanley, "Validation of transcranial Doppler ultrasound with a stereotactic neurosurgical technique," *J. Neurosurg.* **82**, 972–975 (1995).
- ⁴⁸J. Koivukangas, J. Ylitalo, E. Alasaarela, and A. Lauriamen, "Three-dimensional ultrasound imaging of brain for neurosurgery," *Ann. Clin. Res.* **18**, 65–72 (1986).
- ⁴⁹A. Hartov, S. D. Eisner, D. W. Roberts, K. D. Paulsen, L. A. Platenik, and M. L. Miga, "Error analysis for a free-hand three-dimensional ultrasound system for neuronavigation," *Neurosurgical Focus* **6**, Article 5 (1999).
- ⁵⁰R. W. Prager, R. N. Rohling, A. H. Gee, and L. Berman, "Rapid calibration for 3-D freehand ultrasound," *Ultrasound Med. Biol.* **24**, 855–869 (1998).
- ⁵¹S. Tong, D. B. Downey, H. N. Cardinal, and L. Berman, "A three-dimensional ultrasound prostate imaging system," *Ultrasound Med. Biol.* **22**, 735–746 (1996).
- ⁵²D. G. Gobbi, R. M. Comeau, and T. M. Peters, "Ultrasound probe tracking for real-time ultrasound/MRI overlay and visualization of brain shift," presented at the MICCAI 1999, Cambridge, UK, 1999.
- ⁵³K. S. Arun, T. S. Huang, and S. D. Blostein, "Least-squares fitting of two 3-D point sets," *IEEE Trans. Pattern Anal. Mach. Intell.* **PAMI-9**, 698–700 (1987).
- ⁵⁴K. C. Chu and B. K. Rutt, "Polyvinyl alcohol cryogel: An ideal phantom material for MR studies of arterial flow and elasticity," *Magn. Reson. Med.* **37**, 314–319 (1997).
- ⁵⁵R. M. Comeau, A. Fenster, and T. M. Peters, "Integrated MR and ultrasound imaging for improved image guidance in neurosurgery," *SPIE Image Processing* **3338**, 747–754 (1998).
- ⁵⁶W. Birkfellner, F. Watzinger, F. Wanschitz, G. Enislides, C. Kollmann, D. Rafolt, R. Nowotny, R. Ewers, and H. Bergmann, "Systematic distortions in magnetic position digitizers," *Med. Phys.* **25**, 2242–2248 (1998).
- ⁵⁷F. L. Bookstein, "Principal warps: Thin-plate splines and the decomposition of deformations," *IEEE Trans. Pattern Anal. Mach. Intell.* 567–585 (1989).
- ⁵⁸P. J. Edwards, D. L. Hill, J. A. Little, and D. J. Hawkes, "A three-component deformation model for image-guided surgery," *Medical Image Analysis* **2**, 355–367 (1998).
- ⁵⁹N. L. Dorward, O. Alberti, B. Velani, F. A. Gerritsen, W. F. Harkness, N. D. Kitchen, and D. G. Thomas, "Postimaging brain distortion: magnitude, correlates, and impact on neuronavigation," *J. Neurosurg.* **88**, 656–662 (1998).
- ⁶⁰J. M. Fitzpatrick, J. B. West, and C. R. Maurer, Jr, "Predicting Error in Rigid-Body Point Based Registration," *IEEE Trans. Med. Imaging* **17**, 694–702 (1998).
- ⁶¹F. W. Kremkau, in *Diagnostic Ultrasound Principles and Instruments* (W. B. Saunders, Philadelphia, 1993), pp. 18.